VTI migration velocity analysis using RTM

Yunyue (Elita) Li, Peng Shen and Colin Perkins

ABSTRACT

We use a vertical transverse isotropic (VTI) two-way propagation engine to perform wave-equation migration velocity analysis. Using reverse time migration (RTM), we have a chance to characterize the wavefields propagating at large angles and to image steeply dipping reflectors. By including VTI Thomsen parameters, we can better describe the properties of the subsurface. We first derive the migration velocity analysis gradient when using a first-order VTI two-way wave-equation. Then, we test our method on a synthetic VTI Marmousi model. The inversion results show that our method can resolve a better velocity model and a better-focused subsurface image.

INTRODUCTION

Velocity model building has been one of the most challenging problems in the seismic exploration industry. Wave-Equation Migration Velocity Analysis (WEMVA) has been widely studied for velocity building and can be implemented either in the data space (Tarantola, 1984; Woodward, 1992) or in the image space (Sava and Biondi, 2004a,b; Shen, 2004; Shen and Symes, 2008; Guerra et al., 2009). Several advantages drive us to use the image-space WEMVA instead of data-space WEMVA (which is also known as Full-Waveform Inversion): 1), migrated image is often much cleaner than the recorded wavefields; 2), the objective function is directly related to the final image; 3), image-space WEMVA can use a less accurate initial solution without encountering the cycle-skipping problems that can plague FWI. In fact, the optimized output of the image-space WEMVA can be used as the input for FWI (Li and Biondi, 2011).

Since first reported in exploration seismology in the 1930s (McCollum and Snell, 1932), anisotropy has become increasingly important in seismic imaging and exploration. The increasing offset and azimuth in data acquisition has heightened the need for anisotropic imaging and model building. Until now, the transverse isotropic (TI) model has been one most commonly used in seismic imaging and has been considered a better description of the subsurface. Li and Biondi (2011) extend the WEMVA framework to VTI media using the one-way wave-equation. However, the one-way wave-equation cannot accurately describe the wave propagation at large angles with respect to vertical, where anisotropy has larger effects. There have been extensive studies on anisotropic RTM with increasingly complex subsurface models (Fletcher

et al., 2009; Zhang and Zhang, 2009), but reliable anisotropic model-building techniques are still needed.

Therefore, we propose an image-space WEMVA method using a VTI two-way wave-equation as the propagation engine, and evaluate the flatness of the RTM images in the angle domain. In this paper, we first derive the gradient of the differential semblance optimization (DSO) objective function with respect to velocity and ϵ using a Lagrangian augmented functional. To resolve the ambiguity between velocity and ϵ and ensure that our model honors the geology, we use a preconditioning inversion scheme. Finally, we test the proposed method on a synthetic VTI Marmousi model.

FIRST-ORDER TWO-WAY VTI WAVE-EQUATION

The first-order two-way VTI wave-equation can be derived from Hooke's law and Newton's law using Thomson anisotropy parameters (ϵ, δ) and setting shear wave velocity $c_s = 0$ (Duveneck et al., 2008). The first-order system reads as follows:

$$\begin{aligned}
\rho\partial_t v_x &= -\partial_x p_H \\
\rho\partial_t v_y &= -\partial_y p_H \\
\rho\partial_t v_z &= -\partial_z p_V \\
\frac{1}{\rho c^2}\partial_t p_V &= -\sqrt{(1+2\delta)}(\partial_x v_x + \partial_y v_y) - \partial_z v_z + f_V \\
\frac{1}{\rho c^2}\partial_t p_H &= -(1+2\epsilon)(\partial_x v_x + \partial_y v_y) - \sqrt{(1+2\delta)}\partial_z v_z + f_H
\end{aligned} \tag{1}$$

where ρ is the density, c is the velocity, (v_x, v_y, v_z) is the particle velocity vector, and p_V and p_H are pressure in the vertical and horizontal directions, respectively. The source term f_V and f_H are defined by the source wavelet $w(t)$ as follows:

$$f_V(t) = f_H(t) = \int_{-\infty}^{\tau} w(\tau)d\tau. \tag{2}$$

It is straightforward to see that when $\rho = 1$, $\epsilon = 0$ and $\delta = 0$, the first-order system 1 is equivalent to the familiar isotropic acoustic second-order wave-equation:

$$\frac{1}{c^2}\partial_t^2 p - \nabla p = w. \tag{3}$$

For simplicity, we can rewrite system 1 in a matrix-vector notation:

$$\mathbf{L}(c)\mathbf{p} = \mathbf{f}, \tag{4}$$

where $\mathbf{p} = (v_x,\ v_y,\ v_z,\ p_V,\ p_H)^T$, $\mathbf{f} = (0,\ 0,\ 0,\ f_V,\ f_H)^T$, and

$$\mathbf{L} = \begin{vmatrix}
\partial_t & 0 & 0 & 0 & \partial_x \\
0 & \partial_t & 0 & 0 & \partial_y \\
0 & 0 & \partial_t & \partial_z & 0 \\
\sqrt{1+2\delta}\partial_x & \sqrt{1+2\delta}\partial_y & \partial_z & \frac{1}{c^2}\partial_t & 0 \\
(1+2\epsilon)\partial_x & (1+2\epsilon)\partial_y & \sqrt{1+2\delta}\partial_z & 0 & \frac{1}{c^2}\partial_t
\end{vmatrix}. \tag{5}$$

VTI REVERSE-TIME MIGRATION IMAGING CONDITION

Traditionally, the subsurface image is often considered as the first gradient of an FWI objective function with respect to velocity. In this paper, we are going to derive the VTI reverse-time migration imaging condition according to the same criteria.

We define FWI objective function as

$$J_{\rm W} = \frac{1}{2}\langle d - d_{\rm est}, d - d_{\rm est}\rangle, \tag{6}$$

where $d_{\rm est}$ is the data estimated from the current model, which is sampled from wavefield $\mathbf{p}$, and d is the recorded data.

For the first iteration, $d_{\rm est} = 0$. Therefore the first gradient in velocity is:

$$\begin{aligned} \nabla_c J_{\rm W} &= \left(\frac{\partial \mathbf{p}}{\partial c}\right)^* d \\ &= (-\mathbf{L}^{-1}\frac{\partial \mathbf{L}}{\partial c}\mathbf{L}^{-1} f)^* d. \end{aligned} \tag{7}$$

Now we introduce the receiver vector field $\mathbf{q} = (u_x,\ u_y,\ u_z,\ q_V,\ q_H)^T$, which is the solution of the following equation:

$$\mathbf{L}^*(c)\mathbf{q} = \mathbf{f}\ '. \tag{8}$$

The equivalent source term in equation 8 is defined as $\mathbf{f}\ ' = (0,\ 0,\ 0,\ f'_V,\ f'_H)^T$, where $f'_V = f'_H = d$. From equation 5, we have

$$\frac{\partial \mathbf{L}}{\partial c} = \begin{vmatrix} 0 & 0 & 0 & 0 & 0 \\ 0 & 0 & 0 & 0 & 0 \\ 0 & 0 & 0 & 0 & 0 \\ 0 & 0 & 0 & -\frac{2}{c^3}\partial_t & 0 \\ 0 & 0 & 0 & 0 & -\frac{2}{c^3}\partial_t \end{vmatrix}, \tag{9}$$

If we plug equation 8 and 9 into equation 7 and ignore the velocity dependence, we arrive at the imaging condition as follows:

$$\begin{aligned} I &= \mathbf{p}^*\mathbf{M}^*\mathbf{q}, \\ &= (\mathbf{M}\mathbf{p})^*\mathbf{q}, \end{aligned} \tag{10}$$

where

$$\mathbf{M} = \begin{vmatrix} 0 & 0 & 0 & 0 & 0 \\ 0 & 0 & 0 & 0 & 0 \\ 0 & 0 & 0 & 0 & 0 \\ 0 & 0 & 0 & \frac{1}{2}\partial_t & 0 \\ 0 & 0 & 0 & 0 & \frac{1}{2}\partial_t \end{vmatrix}. \tag{11}$$

The explicit form of this imaging condition for acoustic RTM is:

$$I = \int_0^{t_{max}} \frac{1}{2} \left((\partial t p_H) q_H + (\partial t p_V) q_V \right) dt. \tag{12}$$

The scaling factor $\frac{1}{2}$ is chosen to make sure that when $p_H = p_V$, equation 12 reduces to the isotropic cross-correlation imaging condition (Claerbout, 1987). For the purpose of velocity analysis, we often work with extended images and generalized imaging conditions. Similarly, we define our subsurface-offset-domain common-image gathers (SODCIGs) $\mathbf{I}$ as a column vector:

$$\mathbf{I} = [I_{-\mathbf{h}_{\max}}, I_{-\mathbf{h}_{\max}+\Delta\mathbf{h}}, \cdots, I_{\mathbf{0}}, \cdots, I_{\mathbf{h}_{\max}-\Delta\mathbf{h}}, I_{\mathbf{h}_{\max}}]^*, \tag{13}$$

where $\mathbf{h}$ is the half-subsurface offset, which ranges from $-\mathbf{h}_{\max}$ to $\mathbf{h}_{\max}$ with an increment of $\Delta\mathbf{h}$. For each element $I_{\mathbf{h}}$, the extended imaging condition is as follows (Sava and Formel, 2006) :

$$I_{\mathbf{h}} = (\mathbf{S}_{+\mathbf{h}}\mathbf{p})^* \mathbf{M}^* (\mathbf{S}_{-\mathbf{h}}\mathbf{q}), \tag{14}$$

where $\mathbf{S}_{+\mathbf{h}}$ is a shifting operator which shifts the wavefield by an amount of $+\mathbf{h}$ in the $\mathbf{x}$ direction. Notice that $(\mathbf{S}_{+\mathbf{h}})^* = \mathbf{S}_{-\mathbf{h}}$.

MIGRATION VELOCITY ANALYSIS GRADIENTS

In this section, we derive the MVA gradients of objective function 15 by two different approaches: the adjoint method from the perturbation theory, and the Lagrangian augmented function.

WEMVA is a non-linear inversion process that aims to find the velocity model that minimizes the residual field $\Delta\mathbf{I}$ in the image space. Without losing any generality, we define our objective function by DSO (Shen and Symes, 2008) in the subsurface offset domain:

$$J = \frac{1}{2} \sum_{\mathbf{h}} \langle \mathbf{h} I_{\mathbf{h}}, \mathbf{h} I_{\mathbf{h}} \rangle. \tag{15}$$

Although we don't use this DSO objective function in the example, the derivation follows the same logic, and readers can easily substitute their desired image-space objective function into the derivation.

Adjoint method from the perturbation theory

A perturbation, δc, of the velocity model c, induces a perturbation $\delta\mathbf{p}$ in the source wavefield vector $\mathbf{p}$, a perturbation $\delta\mathbf{q}$ in the receiver wavefield vector $\mathbf{q}$, a perturbation $\delta\mathbf{I}$ in the extended image cube $\mathbf{I}$, and hence a perturbation δJ in the objective function J. To the first order and using chain rule, δJ and δc have following relationship:

$$\delta J = \sum_{\mathbf{h}} \frac{\partial J}{\partial I_{\mathbf{h}}} \frac{\partial I_{\mathbf{h}}}{\partial \mathbf{p}} \frac{\partial \mathbf{p}}{\partial c} \delta c + \sum_{\mathbf{h}} \frac{\partial J}{\partial I_{\mathbf{h}}} \frac{\partial I_{\mathbf{h}}}{\partial \mathbf{q}} \frac{\partial \mathbf{q}}{\partial c} \delta c. \tag{16}$$

Now we can define the gradient by the back-projection of a unit perturbation in the objective function:

$$\begin{aligned}\nabla_c J &= \sum_{\mathbf{h}} \left(\frac{\partial J}{\partial I_{\mathbf{h}}}\frac{\partial I_{\mathbf{h}}}{\partial \mathbf{p}}\frac{\partial \mathbf{p}}{\partial c}\right)^* + \sum_{\mathbf{h}} \left(\frac{\partial J}{\partial I_{\mathbf{h}}}\frac{\partial I_{\mathbf{h}}}{\partial \mathbf{q}}\frac{\partial \mathbf{q}}{\partial c}\right)^* \\ &= (\nabla_c J)_1 + (\nabla_c J)_2 \,. \end{aligned} \tag{17}$$

Let's analyze the first term in equation 17 in detail, and the second term follows the same reasoning.

$$\begin{aligned}(\nabla_c J)_1 &= \sum_{\mathbf{h}} \left(\frac{\partial J}{\partial I_{\mathbf{h}}}\frac{\partial I_{\mathbf{h}}}{\partial \mathbf{p}}\frac{\partial \mathbf{p}}{\partial c}\right)^* \\ &= \sum_{\mathbf{h}} \left(\frac{\partial \mathbf{p}}{\partial c}\right)^* \left(\frac{\partial I_{\mathbf{h}}}{\partial \mathbf{p}}\right)^* \left(\frac{\partial J}{\partial I_{\mathbf{h}}}\right)^* \\ &= \sum_{\mathbf{h}} \mathbf{p}^* \left(-\frac{\partial \mathbf{L}}{\partial c}\right)^* \mathbf{L}^{-*} \left(\frac{\partial I_{\mathbf{h}}}{\partial \mathbf{p}}\right)^* \left(\frac{\partial J}{\partial I_{\mathbf{h}}}\right)^* \\ &= \mathbf{p}^* \left(-\frac{\partial \mathbf{L}}{\partial c}\right)^* \mathbf{L}^{-*} \sum_{\mathbf{h}} \left(\frac{\partial I_{\mathbf{h}}}{\partial \mathbf{p}}\right)^* \left(\frac{\partial J}{\partial I_{\mathbf{h}}}\right)^* \end{aligned} \tag{18}$$

where

$$\left(\frac{\partial J}{\partial I_{\mathbf{h}}}\right)^* = \mathbf{h}^* \mathbf{h} I_{\mathbf{h}}, \tag{19}$$

and

$$\begin{aligned}\left(\frac{\partial I_{\mathbf{h}}}{\partial \mathbf{p}}\right)^* &= (\mathbf{S}_{+\mathbf{h}})^* \mathbf{M}^* (\mathbf{S}_{-\mathbf{h}} \mathbf{q}) \\ &= \mathbf{S}_{-\mathbf{h}} \mathbf{M}^* (\mathbf{S}_{-\mathbf{h}} \mathbf{q}). \end{aligned} \tag{20}$$

Plugging equation 19 and 20 into equation 18, we can rewrite equation 18 explicitly as follows:

$$\left(\frac{\partial J}{\partial c}\right)_1 = \mathbf{p}^* \left(-\frac{\partial \mathbf{L}}{\partial c}\right)^* \mathbf{L}^{-*} \sum_{\mathbf{h}} \mathbf{S}_{-\mathbf{h}} \mathbf{M}^* (\mathbf{S}_{-\mathbf{h}} \mathbf{q}) \mathbf{h}^2 I_{\mathbf{h}} \tag{21}$$

Similarly, we can obtain the explicit form for the second term in equation 17:

$$\left(\frac{\partial J}{\partial c}\right)_2 = \mathbf{q}^* \left(-\frac{\partial \mathbf{L}}{\partial c}\right) \mathbf{L}^{-1} \sum_{\mathbf{h}} \mathbf{S}_{+\mathbf{h}} \mathbf{M} (\mathbf{S}_{+\mathbf{h}} \mathbf{p}) \mathbf{h}^2 I_{\mathbf{h}} \tag{22}$$

Substituting equation 21 and equation 22 for the corresponding terms in equation 17, we now have derived the explicit form for the DSO gradient.

Lagrangian augmented functional method

We are now going to use the recipe with the augmented functional that Plessix (2006) provides to derive the image-space DSO gradient. First, let us form the Lagrangian augmented functional, $\mathcal{L}$:

$$\begin{aligned}\mathcal{L}(\mathbf{p},\mathbf{q},I_{\mathbf{h}},\lambda,\mu,\gamma_{\mathbf{h}},c) = & \\ \sum_{\mathbf{h}} \frac{1}{2}\langle \mathbf{h}\ I_{\mathbf{h}},\ \mathbf{h}\ I_{\mathbf{h}}\rangle & \\ +\langle \lambda,\ \mathbf{f}-\mathbf{L}(\mathbf{c})\mathbf{p}\rangle & \\ +\langle \mu,\ \mathbf{f}\ '-\mathbf{L}^*(\mathbf{c})\mathbf{q}\rangle & \\ +\sum_{\mathbf{h}}\langle \gamma_{\mathbf{h}},\ (\mathbf{S}_{+\mathbf{h}}\mathbf{p})^*\mathbf{M}^*(\mathbf{S}_{-\mathbf{h}}\mathbf{q})-I_{\mathbf{h}}\rangle & \end{aligned} \tag{23}$$

Then the adjoint state equations are obtained by taking the derivative of $\mathcal{L}$ with respect to state variables $\mathbf{p}$, $\mathbf{q}$ and $I_{\mathbf{h}}$:

$$\frac{\partial \mathcal{L}}{\partial \mathbf{p}} = -\mathbf{L}^*(c)\lambda + \sum_{\mathbf{h}}(\mathbf{S}_{+\mathbf{h}})^*\mathbf{M}^*(\mathbf{S}_{-\mathbf{h}}\mathbf{q})\gamma_{\mathbf{h}} = \mathbf{0}, \tag{25}$$

$$\frac{\partial \mathcal{L}}{\partial \mathbf{q}} = -\mathbf{L}(c)\mu + \sum_{\mathbf{h}}(\mathbf{S}_{-\mathbf{h}})^*\mathbf{M}(\mathbf{S}_{+\mathbf{h}}\mathbf{p})\gamma_{\mathbf{h}} = \mathbf{0}, \tag{26}$$

$$\frac{\partial \mathcal{L}}{\partial I_{\mathbf{h}}} = -\gamma_{\mathbf{h}} + \mathbf{h}^2 I_{\mathbf{h}} = 0, \forall\ \mathbf{h}. \tag{27}$$

Equation 25, 26, 27 are the adjoint-state equations. Variables $\lambda = (\lambda_x, \lambda_y, \lambda_z, \lambda_V, \lambda_H)^T$ and $\mu = (\mu_x, \mu_y, \mu_z, \mu_V, \mu_H)^T$ are the adjoint-state fields and the solution of the adjoint-state equations 25 and 26. Variable $\gamma_{\mathbf{h}}$ is the scaled image slice at the subsurface offset $\mathbf{h}$.

Now the gradient of the objective function 15 with respect to velocity is:

$$\begin{aligned}\nabla_c J &= \left\langle \lambda,\ -\frac{\partial \mathbf{L}}{\partial \mathbf{c}}\mathbf{p}\right\rangle + \left\langle \mu,\ -\frac{\partial \mathbf{L}^*}{\partial \mathbf{c}}\mathbf{q}\right\rangle \\ &= \left(-\frac{\partial \mathbf{L}}{\partial c}\mathbf{p}\right)^*\lambda + \left(-\frac{\partial \mathbf{L}^*}{\partial \mathbf{c}}\mathbf{q}\right)^*\mu,\end{aligned} \tag{28}$$

If we combine equations 25, 26, and 27 with equation 28, we will arrive at the same solution as in the previous section.

Extension to update anisotropic parameters

The extension from isotropic model updates to anisotropic updates is straightforward. Built on the derivations in the last section, we can easily get the gradients for

anisotropic parameters ϵ and δ as follows:

$$\begin{aligned}\nabla_\epsilon J &= \left\langle \lambda,\ -\frac{\partial \mathbf{L}}{\partial \epsilon}\mathbf{p} \right\rangle + \left\langle \mu,\ -\frac{\partial \mathbf{L}^*}{\partial \epsilon}\mathbf{q} \right\rangle \\ &= \left(-\frac{\partial \mathbf{L}}{\partial \epsilon}\mathbf{p}\right)^* \lambda + \mathbf{q}^* \left(-\frac{\partial \mathbf{L}}{\partial \epsilon}\right) \mu, \end{aligned} \tag{29}$$

$$\begin{aligned}\nabla_\delta J &= \left\langle \lambda,\ -\frac{\partial \mathbf{L}}{\partial \delta}\mathbf{p} \right\rangle + \left\langle \mu,\ -\frac{\partial \mathbf{L}^*}{\partial \delta}\mathbf{q} \right\rangle \\ &= \left(-\frac{\partial \mathbf{L}}{\partial \delta}\mathbf{p}\right)^* \lambda + \mathbf{q}^* \left(-\frac{\partial \mathbf{L}}{\partial \delta}\right) \mu, \end{aligned} \tag{30}$$

where

$$\frac{\partial \mathbf{L}}{\partial \epsilon} = \begin{vmatrix} 0 & 0 & 0 & 0 & 0 \\ 0 & 0 & 0 & 0 & 0 \\ 0 & 0 & 0 & 0 & 0 \\ 0 & 0 & 0 & 0 & 0 \\ 2\partial_x & 2\partial_y & 0 & 0 & 0 \end{vmatrix}, \tag{31}$$

$$\frac{\partial \mathbf{L}}{\partial \delta} = \begin{vmatrix} 0 & 0 & 0 & 0 & 0 \\ 0 & 0 & 0 & 0 & 0 \\ 0 & 0 & 0 & 0 & 0 \\ \frac{\partial_x}{\sqrt{1+2\delta}} & \frac{\partial_y}{\sqrt{1+2\delta}} & 0 & 0 & 0 \\ 0 & 0 & \frac{\partial_z}{\sqrt{1+2\delta}} & 0 & 0 \end{vmatrix}. \tag{32}$$

It is well-known that δ is the parameter most poorly constrained by surface seismic. Therefore, in our study, we assume that δ is obtained from well logs or seismic-well ties, and we invert only for velocity and ϵ.

Physical interpretation and implementation of the DSO gradient

In this subsection, we interpret each term in the DSO gradient formulation, and provide the readers with some hints for implementation. We find the Lagrangian formulation is easier to interpret, and readers can clearly relate the corresponding terms to the adjoint formulation. We will only discuss the physical meaning and the implementation for the first term in the gradient (Equation 28 and 25). Then similar reasoning can be argued using reciprocity.

First, for each image slice in the subsurface-offset domain $I_{\mathbf{h}}$, we compute a weighted image $\gamma_{\mathbf{h}}$ using equation 27. Then we move on to equation 25. We can rearrange the independent and commutable operators as follows:

$$\mathbf{L}^*(c)\lambda = \sum_{\mathbf{h}} \mathbf{S}_{-\mathbf{h}} \left(\mathbf{S}_{-\mathbf{h}} \mathbf{M}^* \mathbf{q}\right) \gamma_{\mathbf{h}}. \tag{33}$$

Operator $\mathbf{M}^*$ corresponds to differentiating q_V and q_H once reversely in time and setting u_x, u_y, and u_z fields to zero. Notice that the directions of propagation and differentiation in time of wavefield $\mathbf{q}$ are the same. Therefore, we can compute the time derivative during the same process as the propagation. Then we shift the reverse-time derivative $\mathbf{q}$ by $-\mathbf{h}$ in $\mathbf{x}$, and multiply it with the weighted image $\gamma_{\mathbf{h}}$. This product is shifted again by $-\mathbf{h}$. Finally, we sum over the contributions from all subsurface-offset image slices to get an effective source term $\mathbf{f}_p$. Next, we solve equation 33 for λ backward in time, using $\mathbf{f}_p$ as the source.

At the same time, in equation 28 $-\frac{\partial \mathbf{L}}{\partial c}$ is a sparse matrix, with non-zero elements only for p_V and p_H. We can therefore write everything out explicitly:

$$(\nabla_c J)_1 = \int_0^{t_{max}} \frac{2}{c^3} \left[(\partial_t p_H)\lambda_H + (\partial_t p_V)\lambda_V \right] dt. \tag{34}$$

The explicit forms for the complete gradients are:

$$\begin{aligned} \nabla_c J &= \int_0^{t_{max}} \frac{2}{c^3} \left[(\partial_t p_H)\lambda_H + (\partial_t p_V)\lambda_V \right] dt \\ &+ \int_0^{t_{max}} \frac{2}{c^3} \left[(\partial_t q_H)\mu_H + (\partial_t q_V)\mu_V \right] dt \end{aligned} \tag{35}$$

and

$$\begin{aligned} \nabla_\epsilon J &= -\int_0^{t_{max}} \left[(\partial_x v_x)\lambda_H + (\partial_y v_y)\lambda_H \right] dt \\ &+ \int_0^{t_{max}} \left[(\partial_x q_H)\mu_x + (\partial_y q_H)\mu_y \right] dt. \end{aligned} \tag{36}$$

Preconditioning the DSO gradient

Velocity model building is a highly underdetermined and nonlinear problem. Therefore, prior knowledge of the subsurface is needed to define a plausible subsurface model. In the formulation of Tarantola (1984), prior information is included as the covariance and the mean of the model. In this study, we assume the initial model we use is the mean, and the covariance of the model has two independent components: spatial covariance and collocated cross-parameter covariance (Li et al., 2011). In practice, instead of regularizing the inversion using Tarantola (1984), we use a preconditioning scheme (Claerbout, 2009): smoothing filtering to approximate square-root of the spatial covariance, and a standard-deviation matrix to approximate the square-root of the cross-parameter covariance.

Mathematically, the preconditioned model perturbation $d\mathbf{n}$ of the subsurface is defined as follows:

$$d\mathbf{m} = \mathbf{B}\mathbf{\Sigma} d\mathbf{n}, \tag{37}$$

where $\mathbf{m} = [c\ \epsilon]^T$. The smoothing operator $\mathbf{B}$ is a diagonal matrix:

$$\mathbf{B} = \begin{vmatrix} \mathbf{B}_c & 0 \\ 0 & \mathbf{B}_\epsilon \end{vmatrix}. \tag{38}$$

with different smoothing operators for velocity and ϵ, according to the geological information in the study area. The standard deviation matrix Σ:

$$\mathbf{\Sigma} = \begin{vmatrix} \sigma_{cc} & \sigma_{c\epsilon} \\ \sigma_{\epsilon c} & \sigma_{\epsilon\epsilon} \end{vmatrix}. \tag{39}$$

can be obtained by rock-physics modeling and/or lab measurements (Bachrach et al., 2011; Li et al., 2011).

We call $\mathbf{n}$ the preconditioning variable, and it relates to the original model $\mathbf{m}$ as follows:

$$\mathbf{m} = \mathbf{B\Sigma n} + (\mathbf{m}_0 - \mathbf{B\Sigma n}_0), \tag{40}$$

where $\mathbf{n}_0$ and $\mathbf{m}_0$ are the initial models in preconditioned space and physical space, respectively. Now, the gradient of the objective function 15 with respect to this preconditioning variable $\mathbf{n}$ is

$$\begin{aligned} \nabla_{\mathbf{n}} J &= (\frac{\partial \mathbf{m}}{\partial \mathbf{n}})^* \nabla_{\mathbf{m}} J \\ &= \mathbf{\Sigma}^* \mathbf{B}^* \nabla_{\mathbf{m}} J, \end{aligned} \tag{41}$$

where $\nabla_{\mathbf{m}} J = [\nabla_c J\ \nabla_\epsilon J]^T$.

In a steepest-decent inversion framework, the initial preconditioning model $\mathbf{n}_0$ is obtained by minimizing the following objective function:

$$J_{\text{init}} = \frac{1}{2} \left\langle \mathbf{m}_0 - \mathbf{B\Sigma n}_0, \mathbf{m}_0 - \mathbf{B\Sigma n}_0 \right\rangle. \tag{42}$$

For the i_{th} iteration

$$\mathbf{n}_{i+1} = \mathbf{n}_i + \alpha_i \nabla_{\mathbf{n}} J, \tag{43}$$

$$\begin{aligned} \mathbf{m}_{i+1} &= \mathbf{B\Sigma n}_{i+1} \\ &= \mathbf{B\Sigma n}_i + \alpha_i \mathbf{B\Sigma}\nabla_{\mathbf{n}} J \\ &= \mathbf{m}_i + \alpha_i \mathbf{B\Sigma\Sigma}^* \mathbf{B}^* \nabla_{\mathbf{m}} J. \end{aligned} \tag{44}$$

Equation 44 suggests an interesting consideration in the context of nonlinear inversion: left-multiplying the gradient with a (semi)positive-definite matrix is equivalent to preconditioning with the square-root of the matrix; thus, the resulting direction is still a descent direction (Claerbout, 2009).

NUMERICAL TEST

In this section, we present the tests of our method on a synthetic VTI Marmousi model. We perform the tests in three steps: objective-function test, single parameter inversion, and joint inversion for two parameters.

Objective function test

We test our method on a VTI Marmousi model. First, synthetic Born data is generated using the models in Figures 1 and 2. The maximum offset is 3 km. Next, we perturb the ϵ model (Figure 2(a)) by a very smooth $\delta\epsilon$ field, as shown in Figure 3(a). We change the perturbation from -50% to 50% of the true ϵ model, and calculate the corresponding objective function respectively.

Ideally, we'd like to choose an objective function that reaches a local minimum at the correct model and is quadratic around the correct model, so that a gradient-based inversion scheme is guaranteed to converge. Based on the results, we choose an angle domain objective function instead of the DSO objective function (Equation 15):

$$J = \frac{1}{2}\langle \mathbf{DRI}, \mathbf{DRI} \rangle, \tag{45}$$

where $\mathbf{R}$ is the Radon transform operator, and $\mathbf{D}$ is the derivative operator along the ray-parameter axis.

As shown in Figure 3(b), the angle-domain objective function has a minimum at the correct epsilon model, and has a semi-quadratic shape with respect to the model perturbation. Therefore, this objective function is a good measure of the error in the anisotropic model. Notice that the tilting effect toward negative ϵ perturbation is caused by the limited acquisition geometry. This effect is negligible for velocity perturbation, because velocity has a first-order effect on the flatness of the angle gather, while ϵ's effect is second-order. We can increase the acquisition offset to mitigate this tilting effect and help the inversion.

Single parameter inversion

In this subsection, we invert for the anisotropic parameter ϵ alone. In this test, we model the synthetic data using very smooth ϵ (Figure 4(a)) and δ (Figure 4(b)) models as suggested by many field applications. To better constrain the inversion for ϵ, we also increase the maximum offset in the acquisition to 6 km.

Compared with the true ϵ model, our initial ϵ model (Figure 5(a)) has negative perturbation of about 50% in the shallower part. Because a perfect velocity model is used in this case, the moveout at large angles is so small that it is almost undetectable to human eyes (Figure 5(b)). However, our inversion scheme is very sensitive to the residual moveout and successfully updates the ϵ model in the correct direction. Figure 6 shows the inverted ϵ model and the corresponding angle-domain common-image gathers after 40 iterations. Comparing with the initial angle gathers (Figure 5(b)), we can see that the slightly curving events at large angles are flattened and the inverted ϵ model is closer to the true one.

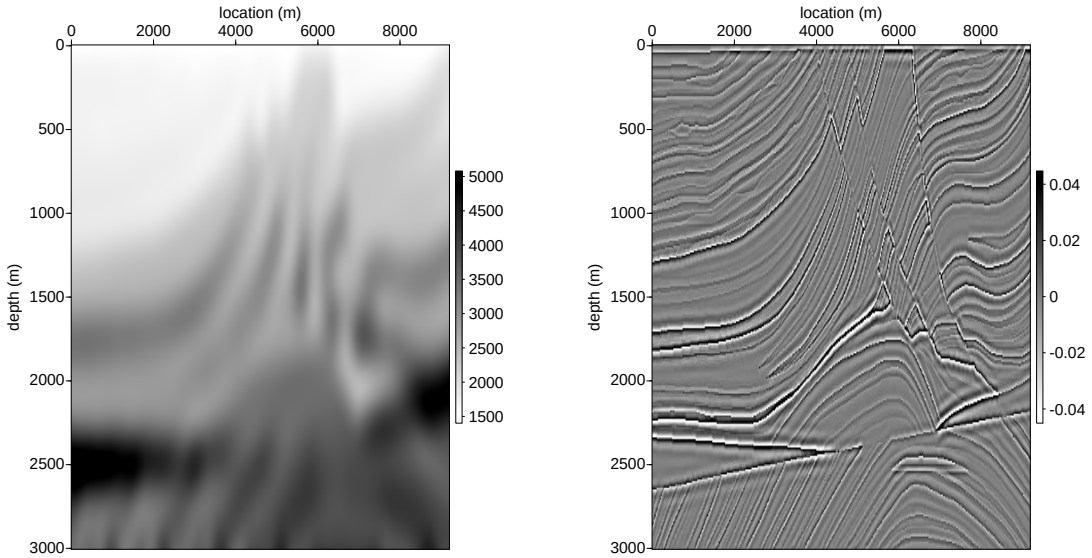

(a) (b)

Figure 1: Smooth velocity model (a) in m/s and reflectivity model (b) used to generate the synthetic Born data. [**CR**]

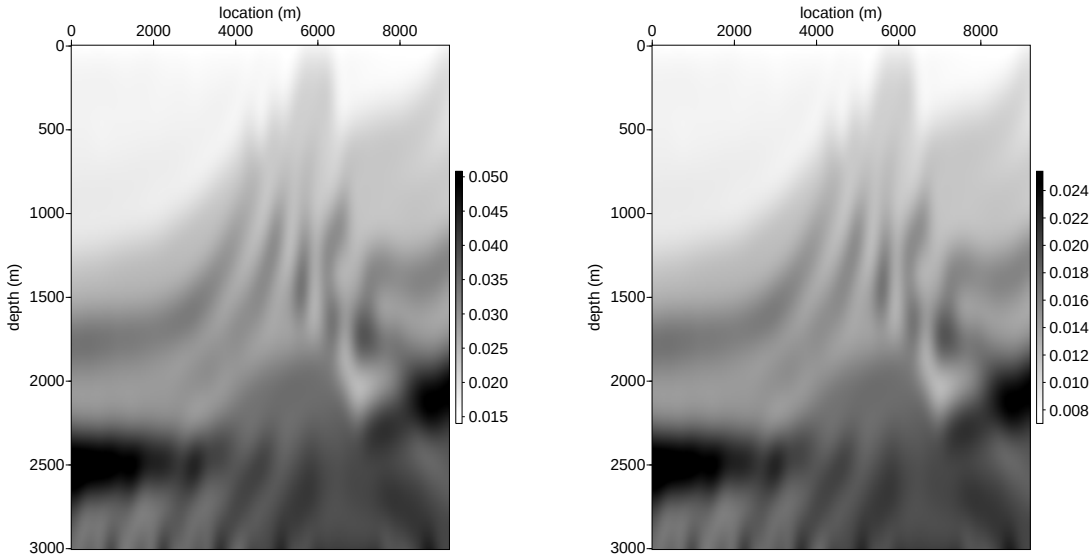

(a) (b)

Figure 2: The ϵ model (a) and δ model (b) used to generate the synthetic Born data. [**CR**]

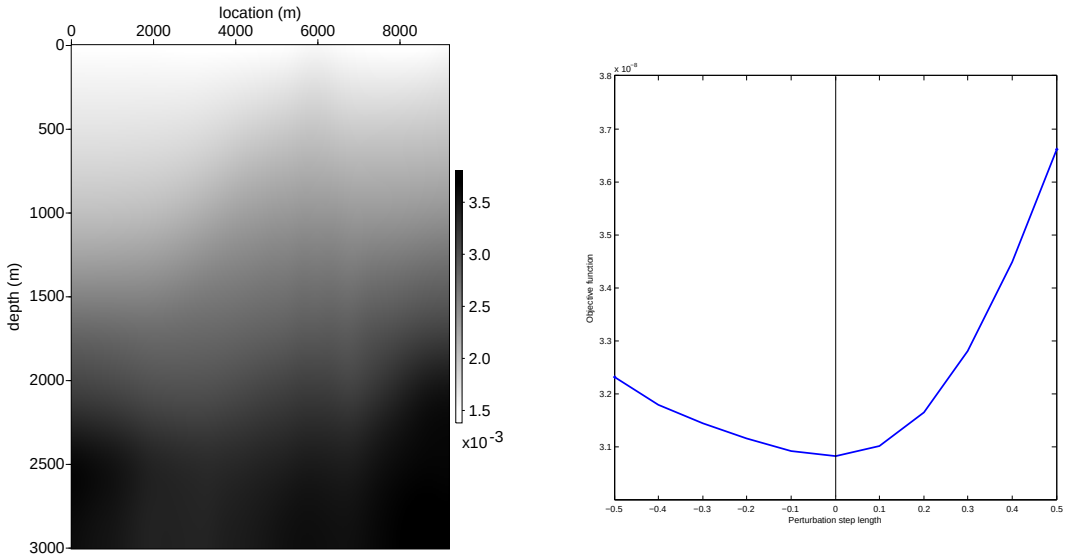

(a) (b)

Figure 3: (a) The $\delta\epsilon$ model to test the objective function. (b) Objective function vs. ϵ perturbation. The angle-domain objective function 45 has a minimum at the correct epsilon model, and has a semi-quadratic shape with respect to the model perturbation. [**CR**]

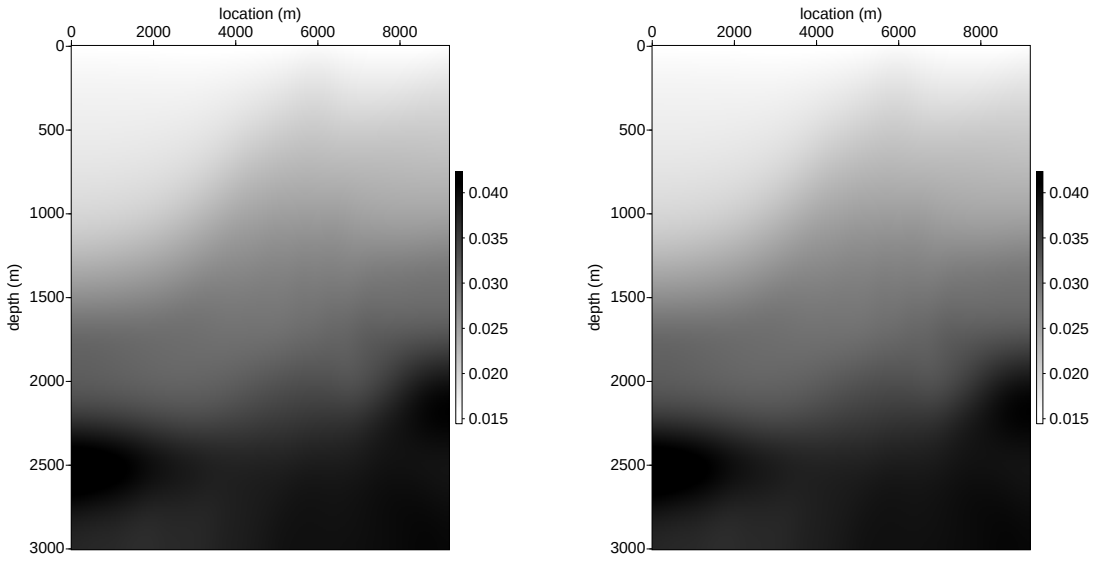

(a) (b)

Figure 4: (a) True ϵ model and (b) true δ model used to generate the synthetic data. [**CR**]

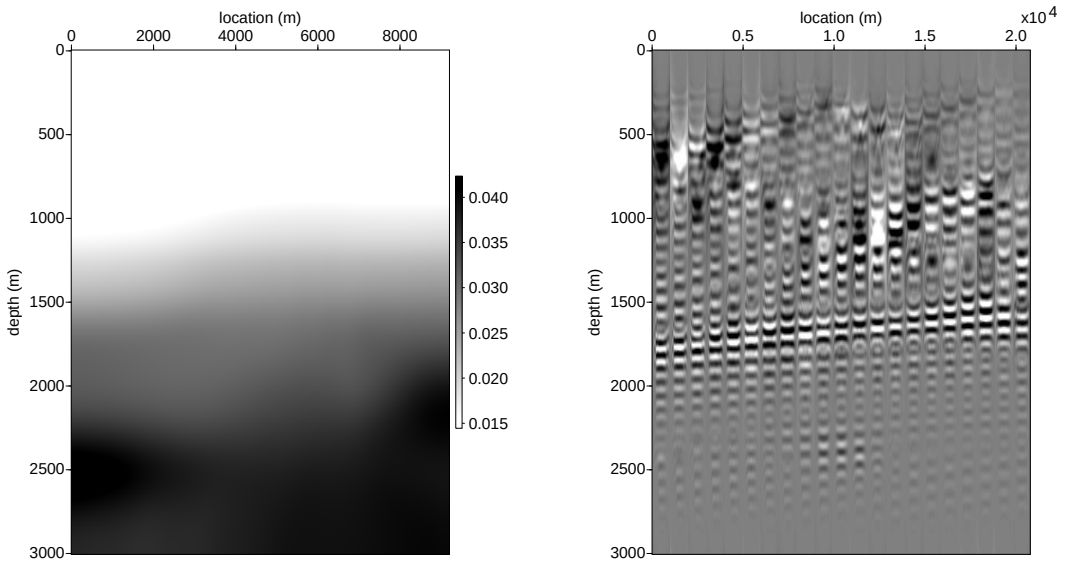

(a) (b)

Figure 5: (a) Initial ϵ model and (b) initial angle-domain common-image gathers using initial ϵ model. Gathers are taken at every 10 common image point from $x = 4$ km to $x = 8$ km. [**CR**]

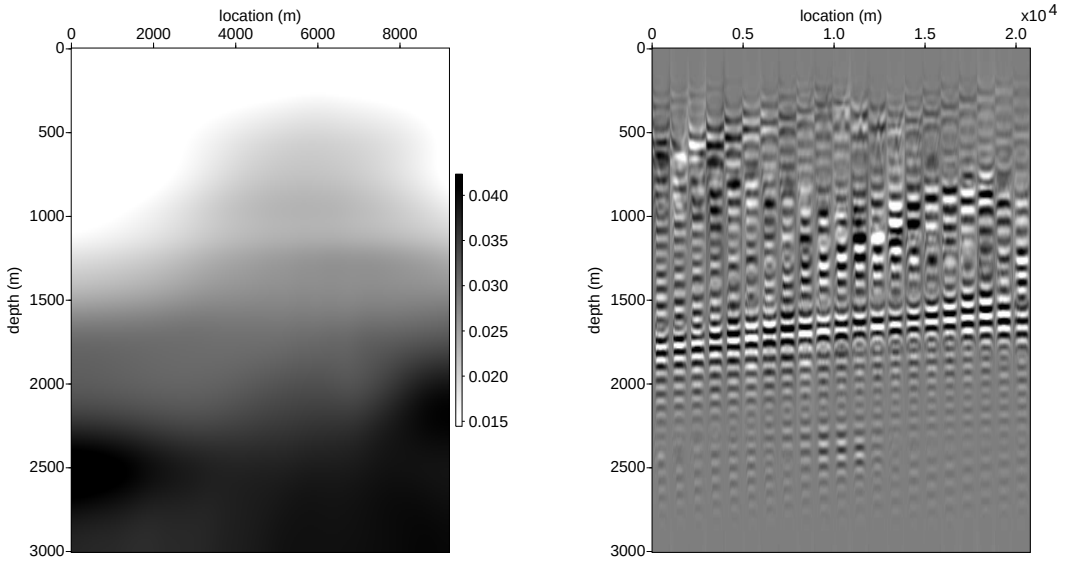

(a) (b)

Figure 6: (a) Inverted ϵ model and (b) final angle-domain common-image gathers using inverted ϵ model in (a). Compared with Figure 5(b), panel (b) shows more even energy across different angles. Gathers are taken at every 10 common image point from $x = 4$ km to $x = 8$ km. [**CR**]

Joint inversion for two parameters

The tests in the previous sections show that we have a reliable objective function and successful inversion results for a single parameter. However, joint inversion for more than one parameter for each grid in the subsurface is far more challenging because of the ambiguity between parameters. As a result, the preconditioning scheme using geological and rock-physics information is crucial for its success.

In this test, we use the same synthetic data as in the last section. Unlike in the last example where we use the perfect velocity model, the starting models for velocity and ϵ are both inaccurate. The initial velocity model and ϵ model are shown in Figures 7(a) and 5(a), respectively. The angle gathers generated using these initial models are shown in Figure 7(b). Significant moveout in the angle-gather events indicates that the initial model is far from the true model. In fact, the initial velocity has a maximum of 15% error compared with the true velocity (Figure 1(a)), while the initial ϵ is about 50% smaller than the true value in the shallow part of the model. Notice that the error in velocity has a much larger effect on the kinematics of the seismic wave, hence a larger effect on the flatness in the angle domain.

After 40 iterations, we obtain the inverted velocity and ϵ models as shown in Figure 8(a) and 8(b). Comparing Figure 8(a) with Figure 1(a), we can conclude that the inversion has successfully recovered the high-resolution vertical structure in the shallow part of the model. Due to the limited illumination, the steep structure in the deeper part of the model is not well resolved. Comparing Figure 6(a) and Figure 8(b), we notice that, because of the error in velocity, the inversion does not converge to the same solution. This is an indication that we have not completely resolved the ambiguity between velocity and ϵ.

Angle gathers generated by the inverted model are shown in Figure 8(c). They are extracted from the same common-image points as in Figure 7(b). The improved model flattens the gathers across the whole section. Notice that the low-frequency energy in the water is the commonly seen wave-path energy for RTM images.

CONCLUSIONS

In this paper, we define an image-space inverse problem to solve for an optimized anisotropy model. To better describe the properties of the subsurface and the wave propagation, we use the first-order VTI two-way wave equation to compute our Green's function. Test results on objective function show that flatness in the angle domain is a valid measure of both velocity and anisotropic parameter ϵ. The results of single-parameter and joint inversions demonstrate that we have successfully resolved the high-frequency structure in velocity and successfully improved the anisotropic model where we have enough angle coverage. The updated image has flattened the gathers in the angle domain.

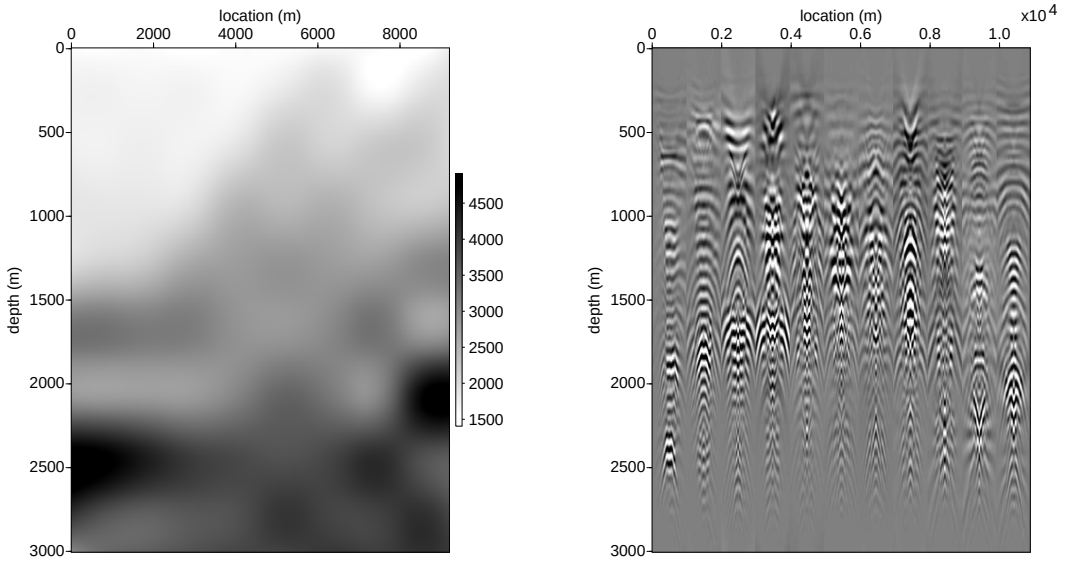

(a) (b)

Figure 7: Initial velocity model (a) in m/s and the angle gathers (b) obtained using initial velocity model. Initial ϵ model is shown in Figure 5(a). Model error causes significant curvatures in the angle gathers. Gathers are taken every 100 common image points from $x = 0$ km to $x = 9$ km. [**CR**]

ACKNOWLEDGEMENT

This work was completed during my internship with Shell in the summer of 2011. The results were produced based on the previous C library for isotropic MVA. We thank Shell International Exploration and Production Company for permission to publish this paper. Yunyue Li thanks the sponsor of the Stanford Exploration Project for their financial support. Yunyue Li dedicates her special thanks to Peng Shen for his previous work and his help throughout her internship.

REFERENCES

Bachrach, R., Y. K. Liu, M. Woodward, O. Zradrova, Y. Yang, and K. Osypov, 2011, Anisotropic velocity model building using rock physics: Comparison of compaction trends and check-shot-derived anisotropy in the Gulf of Mexico: SEG Expanded Abstract, **30**, 207–211.

Claerbout, J., 1987, Imaging the earth's interior: Blackwell Scientific Publications.

Claerbout, J. F., 2009, Image estimation by example.

Duveneck, E., P. Milcik, P. M. Bakker, and C. Perkins, 2008, Acoustic VTI wave equations and their application for anisotropic reverse-time migration: SEG Expanded Abstracts, **27**.

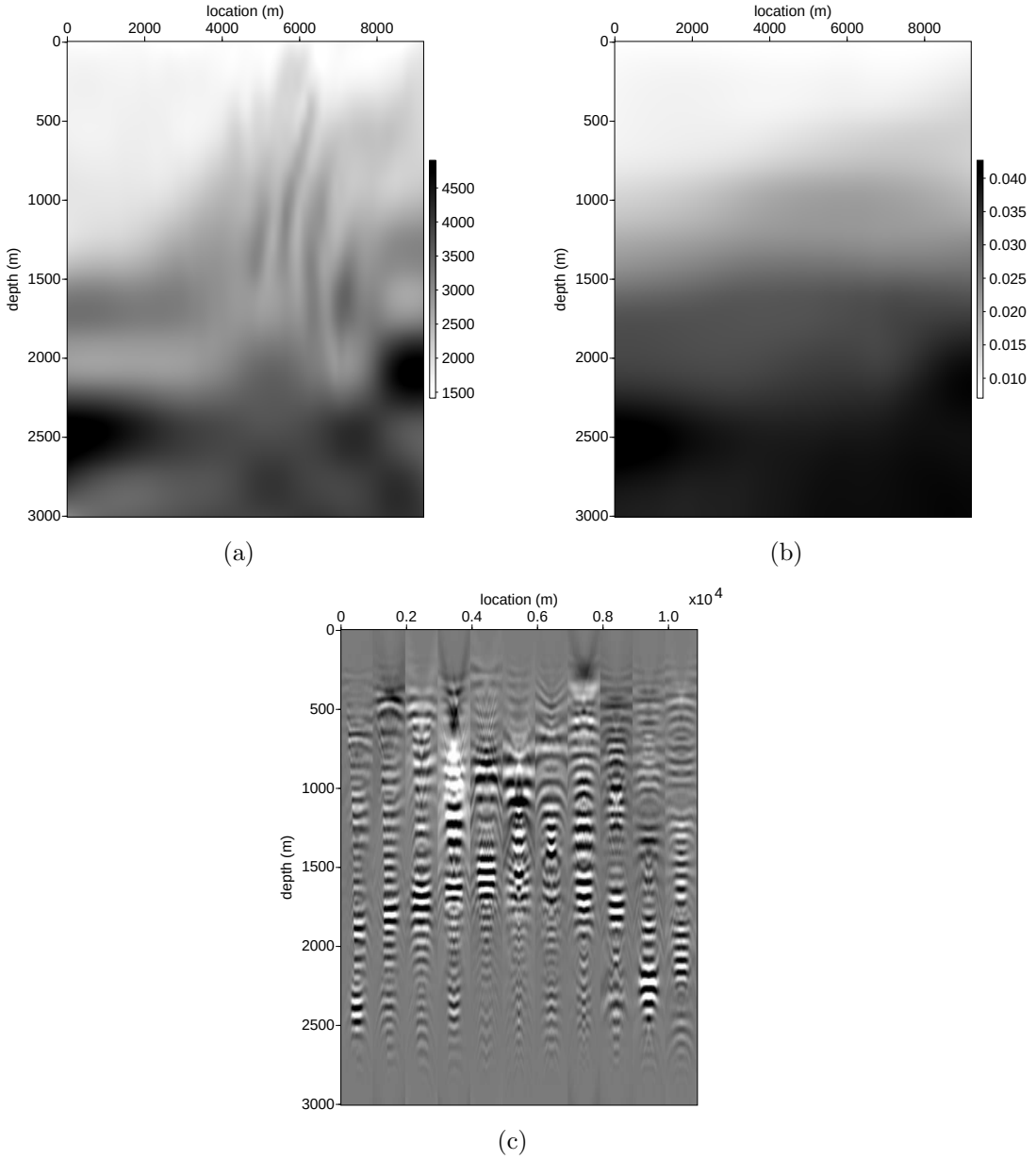

Figure 8: Inverted velocity model (a) in m/s and ϵ model (b) after 40 iterations. Angle gathers (c) obtained by the inverted model. Angle gathers are extracted at the same CIP as those in Figure 7(b). Improved velocity and ϵ flattens the corresponding angle gathers. Gathers are taken every 100 common image points from $x = 0$ km to $x = 9$ km. [**CR**]

Fletcher, R., X. Du, and P. J. Fowler, 2009, Stabilizing acoustic reverse-time migration in TTI media: SEG Expanded Abstracts, **28**.

Guerra, C., Y. Tang, and B. Biondi, 2009, Wave-equation tomography using image-space phase-encoded data: SEP-Report, **138**, 167–180.

Li, Y. and B. Biondi, 2011, Migration velocity analysis for anisotropic models: SEG Expanded Abstract, **30**, 201–206.

Li, Y., D. Nichols, K. Osypov, and R. Bachrach, 2011, Anisotropic tomography using rock physics contraints: 73^{rd} EAGE Conference & Exhibition.

McCollum, B. and F. Snell, 1932, Asymmetry of sound velocity in stratified formations: Physics (Journal of Applied Physics), **2**, 174–185.

Plessix, R.-E., 2006, A review of the adjoint-state method for computing the gradient of a funtional with geophysical applications: Geophysical Journal International, **167**, 495–503.

Sava, P. and B. Biondi, 2004a, Wave-equation migration velocity analysis - I: Theory: Geophysical Prospecting, **52**, 593–606.

———, 2004b, Wave-equation migration velocity analysis - II: Examples: Geophysical Prospecting, **52**, 607–623.

Sava, P. and S. Formel, 2006, Generalized imaging conditions for wave equation migration: CWP Report, **524**.

Shen, P., 2004, Wave-equation migration velocity analysis by differential semblance optimization: PhD thesis, Rice University.

Shen, P. and W. W. Symes, 2008, Automatic velocity analysis via shot profile migration: Geophysics, **73**, VE49–VE59.

Tarantola, A., 1984, Inversion of seismic reflection data in the acoustic approximation: Geophysics, **49**, 1259–1266.

Woodward, M. J., 1992, Wave-equation tomography: Geophysics, **57**, 15–26.

Zhang, Y. and H. Zhang, 2009, A stable TTI reverse time migration and its implementation: SEG Expanded Abstracts, **28**, 3–11.